ROYAL SOCIETY
OF CHEMISTRY

PAPER

Delivery of a system x_c^- inhibitor by a redox-responsive levodopa prodrug nanoassembly for combination ferrotherapy†

Huhu Xin,‡[a] Yong Huang,‡[ab] Honglin Tang,[a] Yuan Chen,[a] Hongguang Xia,*[bc] Fu Zhang,[c] Bowen Li ⓘ *[a] and Yuan Ping ⓘ *[ab]

A comprehensive understanding of ferroptosis signaling pathways significantly contributes to the advances in cancer ferrotherapy. Herein, we constructed a self-assembled prodrug nanosystem targeting system x_c^-, a key regulator for ferroptosis, to amplify the therapeutic efficacy of cancer ferrotherapy. The prodrug nanosystem is assembled between sulfasalazine (SSZ, a ferroptosis resistance inhibitor) and disulfide-bridged levodopa (DSSD) that can chelate Fe^{2+} ions to form SSZ–Fe^{2+}@DSSD, and the resulting nanoassembly can not only inhibit ferroptosis resistance, but also generate ROS in the tumor microenvironment. Whereas the prodrug nanosystem is stable in the physiological environment, it becomes unstable in the tumoral and intracellular reductive microenvironment, where the disulfide linkers are disrupted by high levels of glutathione (GSH), triggering the release of active Fe^{2+} and SSZ. Under the Fenton reaction, the released Fe^{2+} thus can induce ferroptosis, which is amplified by SSZ-mediated inhibition of ferroptosis resistance to synergistically improve the therapeutic efficacy of ferroptosis. Our study thus provides an innovative prodrug strategy to advance anticancer ferroptosis.

1. Introduction

Ferroptosis is a non-apoptotic form of cell death that involves the iron-induced overexpression of reactive oxygen species (ROS).[1,2] During the process of ferroptosis, the presence of hydrogen peroxide in the context of acidic conditions, such as tumoral and inflammatory microenvironments, can accelerate the Fe^{2+}-based Fenton reaction to produce ROS and induce the intracellular lipid peroxidation (LPO), thereby leading to the death of cancer cells.[3,4] As a promising therapeutic modality for cancer treatment, ferrotherapy still suffers from a few drawbacks, such as poor therapeutic efficacy, low tissue specificity, and severe side effects.[5–8] To overcome these obstacles, the development of a ferroptosis inducer that can generate substantial production of hydroxyl radicals (•OH) to induce ferroptosis has attracted much attention.[9] However, the resistance to

ferroptosis, as a consequence of the recovery of intracellular redox homeostasis, is becoming a major issue, often leading to the poor response to cancer ferrotherapy.[10,11] As a consequence, there is still an urgent demand to develop a convenient and safe strategy for inhibiting ROS-depleted pathways and achieving drug release in a controlled manner.

A comprehensive understanding of ferroptosis-related pathways regulating cancer progression has led to tremendous advances in ferrotherapy.[12,13] Since ferroptosis was proposed in 2012, increasing evidence reveals that ferroptosis can be induced by extrinsic or intrinsic pathways.[14] In extrinsic pathways, the glutamate/cystine transporter (system x_c^-), a cell surface amino acid antiporter, can facilitate the transportation of extracellular cystine into cells to produce intracellular cysteine, which serves as one of the synthetic substrates for the antioxidant glutathione (GSH),[10,15] *via* a reductive reaction. GSH is known to be a necessary cofactor for maintaining the normal function of important intrinsic pathways, such as glutathione peroxidase 4 (GPX4) that plays a crucial role in protecting cancer cells against ferroptosis through the inhibition of LPO.[4,16] In the extrinsic–intrinsic pathway (system x_c^--GSH-GPX4), GSH plays an important role and its depletion can down-regulate the GPX4 expression and increase ROS levels.[1–4] Therefore, system x_c^--GSH-GPX4 acts as an attractive target for regulating ferroptosis. In the past decade, several small molecular drugs, such as sorafenib, sulfasalazine and artemisinin,[17,18] have

[a] *College of Pharmaceutical Sciences, Zhejiang University, Hangzhou 310058, China. E-mail: bowen_li@zju.edu.cn, pingy@zju.edu.cn*

[b] *Liangzhu Laboratory, Zhejiang University Medical Center, 1369 West Wenyi Road, Hangzhou 311121, China. E-mail: hongguangxia@zju.edu.cn*

[c] *Department of Biochemistry & Research Center of Clinical Pharmacy of The First Affiliated Hospital, Zhejiang University School of Medicine, Hangzhou 310058, China*

† Electronic supplementary information (ESI) available. See DOI: 10.1039/d1tb00742d

‡ The authors contributed equally to this work.

7172 | *J. Mater. Chem. B*, 2021, **9**, 7172–7181

This journal is © The Royal Society of Chemistry 2021

been demonstrated to inhibit the system x_c^--GSH-GPX4 pathway, and trigger ferroptosis in cancer cells. Sulfasalazine (SSZ) is an FDA-approved anti-inflammatory drug that has been used to treat ulcerative colitis and rheumatoid arthritis.[3] Recently, some reports have revealed that it can act as a system x_c^- inhibitor to reduce the transportation of cystine, and then induce the depletion of GSH in the system x_c^--GSH-GPX4 pathway and inhibit GPX4 expression to alleviate the resistance to ferroptosis.[17–19] However, the undesirable water solubility and metabolic stability of SSZ often compromise its therapeutic efficacy *in vivo*. Thus, improvement in terms of water solubility and metabolic stability for SSZ is necessary.

Recently, iron chelators have emerged as a fascinating class of ferroptosis inducers to improve the intracellular ROS levels.[20–22] Iron chelators usually contain polyphenols and Fe^{2+} that can self-assemble into stable nanoparticles, *via* chelation and hydrophobic interactions.[23] As compared with small molecular inducers, a nanoscaled iron chelator displays good biocompatibility, and its Fenton reaction catalytic activities can be largely reserved until the chelator reaches the tumor tissue. In the tumor microenvironment, such a chelation can be disrupted to release Fe^{2+} by decreased acidic pH, and the release of Fe^{2+} can generate ROS to induce ferroptosis.[24–28] Interestingly, the chelation between polyphenols and Fe^{2+} can be also exploited for the design of stimuli-responsive drug delivery systems,[29–32] which can deliver SSZ and simultaneously generate ROS to inhibit the system x_c^--GSH-GPX4 pathway for combined ferrotherapy.

Herein we report a ferroptosis nano-prodrug that can generate intercellular ROS and inhibit the system x_c^--GSH-GPX4 pathway to enhance the cancer ferrotherapy. As shown in Scheme 1, this nano-prodrug is assembled by disulfide-bridged levodopa (DSSD), a system x_c^- inhibitor SSZ and Fe^{2+}. DSSD is synthesized *via* chemical modification of carboxylic acids on levodopa with a GSH-responsive linker (–SS–), and the nanoparticle (SSZ@DSSD) is formed through the disulfide-facilitated assembly between DSSD and SSZ. Then, the multiple phenolic hydroxyl groups on SSZ@DSSD can chelate Fe^{2+} as a ferroptosis nano-prodrug (SSZ–Fe^{2+}@DSSD). The nano-prodrug is stable in the physiological environment, whereas excessive GSH and acidic microenvironment in tumor tissue breaks the disulfide bridge, thereby disrupting its nanostructure and releasing the system x_c^- inhibitor SSZ and Fe^{2+}. The release process Fe^{2+} can then induce ferroptosis by increasing •OH generation, and SSZ serves as an active inhibitor to block the system x_c^--GSH-GPX4 pathway to alleviate the resistance to ferroptosis. In addition, as nano-prodrug SSZ–Fe^{2+}@DSSD can induce cytotoxicity only against cancer cells, the ferroptosis nano-prodrug that we have designed therefore provides synergistic effects for cancer ferrotherapy.

2. Experimental section

2.1 Materials and instruments

3,4-Dihydroxyphenyl-L-ananine (L-DOPA), 1, 8-diazabicyclo[5.4.0]undec-7-ene (DBU), 2-(7-aza-1*H*-benzotriazole-1-yl)-1,1,3,3-tetramethyluronium
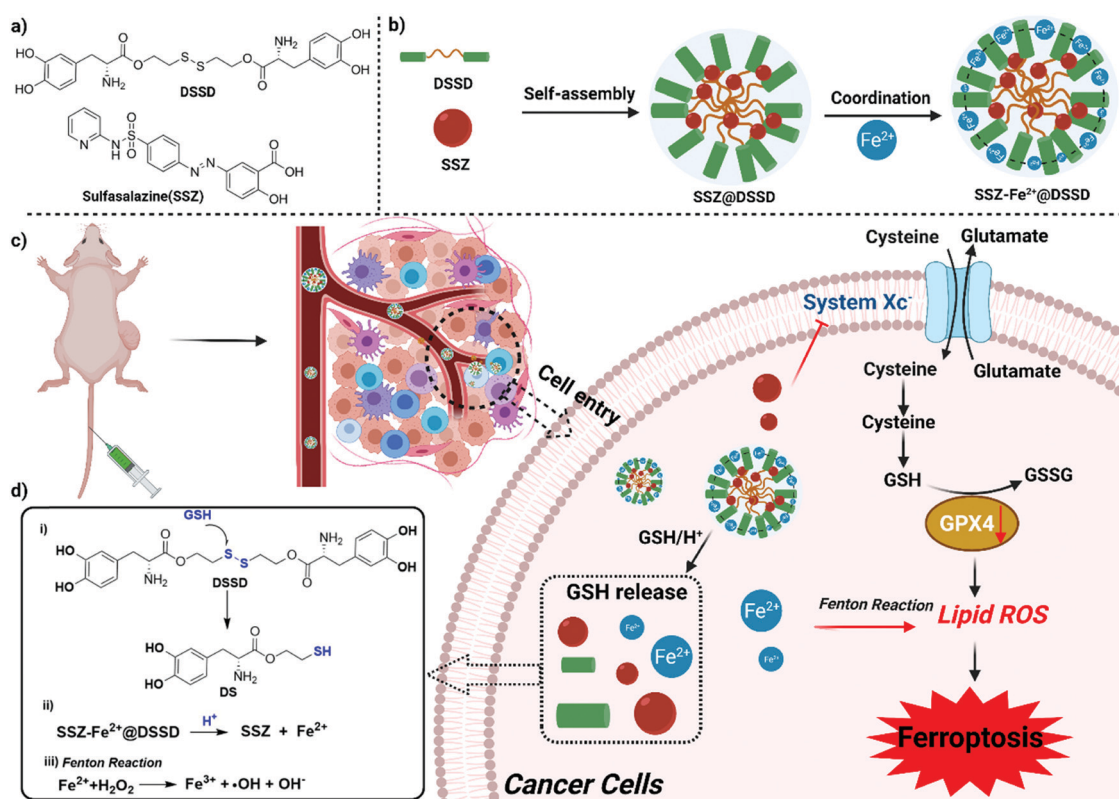
Scheme 1 (a) The chemical structures of DSSD and SSZ. (b) The self-assembly process of SSZ@DSSD and SSZ–Fe^{2+}@DSSD. (c) Schematic illustration for release of SSZ and Fe^{2+} from GSH-responsive nano-prodrug SSZ–Fe^{2+}@DSS and the Ferroptosis-induced therapeutic effect on tumor inhibition. (d) The GSH-responsive and ROS-activation process of SSZ–Fe^{2+}@DSSD.

This journal is © The Royal Society of Chemistry 2021

J. Mater. Chem. B, 2021, 9, 7172–7181 | 7173

hexafluoro-phosphate (HATU), sulfasalazine and *tert*-butyldi-methylsilyl chloride (TBDMSCl) were purchased from Beijing Innochem Science & Technology Co., Ltd. 2-Hydroxyethyl disulphide, di-*tert*-butyl dicarbonate (Boc₂O), sodium hydroxide, *N,N*-diisopropylethylamine (DIPEA), tetrabutylammonium fluoride solution (TBAF, 1.0 M in THF), trifluoroacetic acid, methylene blue (MB), iron(II) chloride (FeCl₂), 2′,7′-dichloro-dihydrofluorescein diacetate (DCFH-DA), 4,6-diamidino-2-phenylindole (DAPI), calcein-AM, propidium iodide (PI) and sodium sulfate anhydrous were purchased from Shanghai Aladdin Biochemical Technology Co., Ltd.

^{1}H NMR spectra were measured on a Bruker Avance 500 MHz NMR spectrometer. High-resolution mass spectra were recorded on an Agilent 6224 Accurate-Mass Time-of-Flight (TOF) LC/MS system. UV-vis spectra were recorded on a Hitachi U-3010 UV-vis spectrophotometer. The fluorescence images were obtained on an Olympus IX71 fluorescence microscope with a DP72 color CCD. The Agilent 1260 was used for high-performance liquid chromatography in HPLC analyses. The morphology of the nanoparticles was determined on a Hitachi HT7700 transmission electron microscope. Zeta potentials of the nanoparticles were measured on a Malvern Zetasizer Nano ZS90.

2.2 The synthetic experiments

Synthesis of DOPA-TB. To a stirred solution of L-DOPA (1.972 g, 10 mmol) in dioxane (5.0 mL) at 0 °C under a nitrogen atmosphere, the Boc₂O (2.4 g, 11 mmol) and 1 M NaOH (11 mL, 11 mmol) were added and the reaction mixture was stirred for overnight at room temperature under a nitrogen atmosphere. After completion of the reaction, the solvent was evaporated under reduced pressure, then the mixture was dissolved in DCM and washed with HCl solution and brine. The organic layer was combined and dried over anhydrous Na₂SO₄, and the solvent was evaporated to obtain DOPA-Boc without further purification.

DOPA-Boc (1.188 g, 4 mmol) was dissolved in 15 mL of anhydrous acetonitrile, followed by addition of TBDMSCl (1.507 g, 10 mmol), and then DBU (1.52 mL, 10 mmol) was slowly added to the reaction solution at 0 °C. The mixture was stirred at room temperature for 16 h and then concentrated under reduced pressure. The residue was purified by column chromatography (DCM : MeOH = 10 : 1 in v/v) to give a yellow oil product DOPA-TB (0.819 g, 39%). ^{1}H NMR (500 MHz, CDCl₃) δ 6.75 (d, J = 8.1 Hz, 1H), 6.67–6.61 (m, 2H), 4.94 (d, J = 7.9 Hz, 1H), 4.54 (dd, J = 12.7, 6.0 Hz, 1H), 3.12–2.91 (m, 2H), 1.42 (s, 9H), 0.98 (d, J = 2.9 Hz, 18H), 0.18 (d, J = 4.7 Hz, 12H). HR-MS (ESI): calcd for $C_{26}H_{47}NNaO_6Si_2^+$ [M + Na]$^+$ 548.2840, found 548.2838.

Synthesis of DSSD-TB. DOPA-TB (680 mg, 1.3 mmol) and HATU (738 mg, 1.95 mmol) were dissolved in 10 mL anhydrous DCM under a nitrogen atmosphere. After 1 h, DIPEA (334 mg, 2.6 mmol) in 5 mL DCM was added and the mixture was stirred for 30 min, then 2-hydroxyethyl disulfide (90 mg, 0.6 mmol) was added to the reaction solution. The reaction mixture was stirred overnight at room temperature under nitrogen atmosphere and extracted with DCM, dried over anhydrous Na₂SO₄ and concentrated. The crude product was purified by column chromatography

(DCM : MeOH = 20 : 1 in v/v) to offer a colorless oil product DSSD-TB (0.331 g, 63%). ^{1}H NMR (500 MHz, CDCl₃) δ 6.73 (d, J = 8.1 Hz, 2H), 6.62 (d, J = 2.1 Hz, 2H), 6.56 (dd, J = 8.1, 1.7 Hz, 2H), 4.95 (d, J = 8.0 Hz, 2H), 4.51 (dd, J = 13.4, 6.0 Hz, 2H), 4.38–4.30 (m, 4H), 2.96 (qd, J = 13.8, 5.7 Hz, 4H), 2.87 (t, J = 6.7 Hz, 4H), 1.42 (s, 18H), 0.97 (t, J = 4.0 Hz, 36H), 0.20–0.17 (m, 24H). HR-MS (ESI): calcd for $C_{56}H_{101}N_2O_{12}S_2Si_4^+$ [M + H]$^+$ 1169.5868, found 1169.5875.

Synthesis of DSSD-B. TBAF (1.25 mL, 1.25 mmol) was added dropwise to the solution of DSSD-TB (292 mg, 0.25 mmol) in THF (5 mL) at 0 °C. After 1 h, the resulting mixture was quenched with saturated ammonium chloride solution (40 mL). The resulting solution was extracted with ethyl acetate and concentrated. The residue was purified by column chromatography (EA : PE = 3 : 1 in v/v) to give a white powder DSSD-B (151 mg, 85%). ^{1}H NMR (500 MHz, CDCl₃) δ 6.79 (d, J = 8.4 Hz, 4H), 6.54 (d, J = 8.0 Hz, 2H), 5.13 (d, J = 8.2 Hz, 2H), 4.48 (dd, J = 16.3, 9.5 Hz, 4H), 4.13 (dd, J = 9.2, 4.8 Hz, 2H), 2.94 (dd, J = 18.9, 10.7 Hz, 4H), 2.87–2.66 (m, 4H), 1.43 (s, 18H). HR-MS (ESI): calcd for $C_{32}H_{45}N_2O_{12}S_2^+$ [M + H]$^+$ 713.2414, $C_{32}H_{44}N_2NaO_{12}S_2^+$ [M + Na]$^+$ 735.2233, found 713.2406, 735.2229.

Synthesis of DSSD. To a mixture of DSSD-B (142 mg, 0.2 mmol) in dichloromethane (5 mL) at 0 °C, the trifluoroacetic acid (2.3 g, 1.5 mmol) in dichloromethane (5 mL) was added dropwise, and then the mixture was reacted at room temperature for 4 h. After that, the mixture was concentrated using the vacuum-rotary evaporation procedure and recrystallized by diethyl ether to get DSSD (95.5 mg, 93.5%). ^{1}H NMR (500 MHz, DMSO) δ 8.98 (s, 4H), 8.39 (s, 4H), 6.68 (d, J = 8.0 Hz, 2H), 6.60 (d, J = 2.0 Hz, 2H), 6.46 (dd, J = 8.0, 2.1 Hz, 2H), 4.42–4.29 (m, 4H), 4.18 (t, J = 6.5 Hz, 2H), 3.00–2.87 (m, 8H). HR-MS (ESI): calcd for $C_{22}H_{29}N_2O_8S_2^+$ [M + H]$^+$ 513.1365, found 513.1364.

2.3 Preparation of SSZ–Fe²⁺@DSSD

The SSZ–Fe^{2+}@DSSD nano-prodrug was prepared *via* the nano-precipitation method. Briefly, DSSD (4 mg) and SSZ (2 mg) were dissolved in 200 μL DMSO. Subsequently, the solution was added into deionized water (10 mL) dropwise under vigorous sonication. Then the mixture was stirred for 1 h at room temperature, and the dispersion was dialysed for 24 h to remove DMSO and excess SSZ, and obtain the SSZ@DSSD nanoparticles. After that FeCl₂ (200 μL, 2 mg mL^{-1}) was added into the SSZ@DSSD under a nitrogen atmosphere and stirred for 2 h. Finally, the SSZ–Fe^{2+}@DSSD nano-prodrug was collected by centrifugation and washed with deionized water for some measurements.

For determination of the SSZ loading, SSZ–Fe^{2+}@DSSD (1 mg) was dissolved in 5 mL DMSO, followed by UV-vis spectroscopy measurements at 361 nm to monitor SSZ. The SSZ loading efficiency was determined based on absorption spectrometry with the experimentally determined calibration curves.

2.4 *In vitro* release of SSZ from SSZ–Fe²⁺@DSSD

The *in vitro* drug release of the samples under different conditions was investigated *via* the dialysis method. A certain

amount of SSZ–Fe^{2+}@DSSD dispersion in dialysis bags (with a cut-off molecular weight of 1000 Da) and placed in 50 mL of different environmental media (the pH condition was adjusted to 7.4, 6.8 and 5.5) with or without GSH at 37 °C. At appropriate time points, 1 mL of the dialysate was taken out and the same amount of fresh medium was added. The amounts of the released SSZ were measured by HPLC.

2.5 Evaluation of •OH generation

To study the •OH generation ability of SSZ–Fe^{2+}@DSSD under different pH conditions, the colorimetric method was employed based on the degradation of MB. Briefly, SSZ–Fe^{2+}@DSSD was added into PBS buffer (pH 7.4 or 6.8) or citric acid–sodium citrate buffer (pH 5.5) containing H$_2$O$_2$ (1 mM) and MB (20 μM) were incubated at 37 °C for 1 h, at different time points, the absorbance change of the incubation solution at 664 nm was monitored to record the degradation percentage of MB.

2.6 Cell culture

The 293T, HeLa and LO2 cells were incubated in DMEM medium, while HepG2 and A549 cells were incubated in RPMI1640 medium, and the above media were supplemented with 10% fetal bovine serum (FBS) at 37 °C in an incubator (containing 5% CO$_2$ gas).

2.7 Cell viability assay

To evaluate the cell cytotoxicity of the different formulation nanoparticles, the HeLa cells and LO2 cells (1 × 10^4 cells per well) were seeded in 96-well plates and incubated for 24 h at 37 °C with 5% CO$_2$. After removal of the medium, the cells were washed with PBS buffer and incubated with different nanoparticles (the levels of SSZ and SSZ–Fe^{2+}@DSSD nano-prodrug were equal) at various concentrations (0, 100, 200, 300, 400 and 500 μg mL^{-1}) for an additional 24 h. After that, the above medium was removed and the cells were washed twice with PBS buffer, and 10 μL freshly prepared CCK8 toxicity test solution was added to each well. After further culturing in an incubator for 4 h, the absorbance value at 450 nm was measured using a Thermo MK3 ELISA reader to quantify the survival rate. Each independent experiment was performed eight times and the cell viability was evaluated by comparison with the negative control.

2.8 Determination of intracellular ROS

The ability for intracellular ROS generation inside different kinds of cells was measured with DCFH-DA. At first, we invested the intracellular ROS of cancer cells and normal cells with SSZ–Fe^{2+}@DSSD. Briefly, cancer cells (HeLa, A549 and HepG2 cells) and normal cells (293T and LO2 cells) were seeded in 6-well plates (1 × 10^5 cells per well) and incubated for 24 h. Then the culture media were removed and fresh medium containing 200 μg mL^{-1} SSZ–Fe^{2+}@DSSD was added. After 6 h of incubation, the cells were washed with PBS three times to remove excess nano-prodrug. After that, the cells were treated with DCFH-DA (20 μM) for another 20 min and washed with PBS buffer. The DCF fluorescence of cells was observed using a

fluorescence microscope. Afterwards, we explored the effect of different nanoparticles on ROS generation. We chose HeLa cells as the model, which were incubated with different formulations of nanoparticles for 6 h and then treated with DCFH-DA for 20 min. Finally, the fluorescence of cells was visualized using a fluorescence microscope.

2.9 Western blot analysis

The HeLa cells (2 × 10^5 cells per well) were seeded in a 6-well plate and incubated with PBS, DSSD, Fe^{2+}, SSZ, SSZ@DSSD or SSZ–Fe^{2+}@DSSD for 24 h. The treated cells were washed with cold PBS and lysed in lysis buffer containing a protease inhibitor, followed by grinding the cells on ice for another 30 min. The cell lysate was centrifuged to collect the supernatant. The protein extracts were resolved by SDS–PAGE and subsequently transferred to polyvinylidene fluoride (PVDF) membranes. After being blocked with bovine serum albumin blocking buffer for 1 h, the membranes were incubated overnight with a primary antibody of GPX4 or GAPDH. Then, the membrane was incubated with peroxidase-conjugated secondary antibodies for 1 h, and immunoreactive bands were detected using the ECL system (Azure Biosystems C150).

2.10 Live/dead cell staining

To further assess the therapeutic effect of the different nanoparticles, the live/dead cell staining assay was used. The HeLa cells (1 × 10^5 cells per well) were seeded in 6-well plates and incubated for 24 h. Then, the fresh medium containing different formulations nanoparticles was added for another 24 h. After that, the cells were coincubated with calcein-AM and PI according to the protocol. The fluorescence imaging of cells was observed *via* a fluorescence microscope.

2.11 *In vivo* antitumor evaluation

Female athymic BALB/c mice (16–20 g, 4–6 weeks old) were housed in a pathogen-free environment at the Laboratory Animal Centre, Zhejiang University, and were supplied with sterilized air, food and water. All animal experiments were performed in accordance with the policies of and approved by the animal ethics committee of Laboratory Animal Welfare and Ethics Committee of Zhejiang University (Approval No.: 18286).

To investigate the antitumor efficiencies of different therapeutic formulations, the HeLa cells were injected into the nude mice to establish a subcutaneous tumor-bearing model. When the tumor volume reached 100 mm^3, the mice were randomly divided into five groups: PBS, DSSD, SSZ, SSZ@DSSD, and SSZ–Fe^{2+}@DSSD, subsequently. The tumor volume (*V*) was estimated as follows: V (mm^3) = length (mm) × width^2 (mm)/2. The mice were intravenously injected with different formulations, which were repeated once every three days five times. The body weights and tumor volumes were recorded every two days. After twenty-eight days of treatment, the mice of each group were sacrificed, and the main organs (heart, liver, spleen, lungs, and kidneys) and tumor were collected for histological analysis. The tumor growth inhibitory rates were calculated as follows:

This journal is © The Royal Society of Chemistry 2021

J. Mater. Chem. B, 2021, **9**, 7172–7181 | **7175**

(mean of control group volume) − (mean of different group volume)/(mean of control group volume) × 100%.

3. Results and discussion

3.1 Self-assembly and characterization of SSZ–Fe^{2+}@DSSD

As shown in Scheme S1 (ESI†), the GSH-responsive compound DSSD was synthesized by covalently linking two L-DOPA with 2-hydroxyethyl disulphide, and the DSSD and all intermediate products were characterized by ^{1}H NMR and HR-MS (Fig. S1–S8, ESI†). The DSSD, SSZ and Fe^{2+} were self-assembled *via* the nano-precipitation method and formed SSZ–Fe^{2+}@DSSD. As shown in Fig. 1a. SSZ was first complexed with DSSD *via* coprecipitation in the aqueous solution to form SSZ@DSSD nanoparticles. Then, the Fe^{2+} was added into the SSZ@DSSD solution under a nitrogen atmosphere to chelate with the polyhydroxy groups of DSSD, and purified the nano-particles by centrifugation for constructing a SSZ–Fe^{2+}@DSSD nano-prodrug. During this process, the particle size and morphology of SSZ@DSSD and SSZ–Fe^{2+}@DSSD were monitored by transmission electronic microscopy (TEM) and dynamic light scattering (DLS), the results were exhibited in Fig. 1b and c.

The hydrodynamic diameter of SSZ@DSSD was about 172.5 nm, and the diameter increased to 212.6 nm after chelating with Fe^{2+} (SSZ–Fe^{2+}@DSSD); both of them showed narrow size distributions, low PDI value and showed obvious Tyndall effect. Meanwhile, the zeta potential of SSZ–Fe^{2+}@DSSD was determined to be −4.3 mV, which was dramatically higher than that of SSZ@DSSD (−20.1 mV), indicating that the Fe^{2+} has been successfully coordinated with polyhydroxy groups. Moreover, the TEM of SSZ@DSSD and SSZ–Fe^{2+}@DSSD were also investigated in Fig. 1b and c, and both of them exhibited a spherical shape with ∼150 nm average size with relatively good uniformity and dispersity. In addition, high-angle annular dark-field scanning transmission electron microscopy (HAADF-STEM) was performed to verify the element distribution of SSZ–Fe^{2+}@DSSD in Fig. S9 (ESI†), and found that the Fe element was overlapped well with S, N, or O and distributed evenly across the whole SSZ–Fe^{2+}@DSSD nano-particles, suggesting the self-assembly feature of the nano-prodrug we have developed. To further evaluate their stability, the size and PDI of SSZ@DSSD and SSZ–Fe^{2+}@DSSD were monitored in PBS buffer for a period of 21 days. As illustrated in Fig. S10 (ESI†), the nanoparticles of SSZ@DSSD were stable

Fig. 1 The self-assembly process and characterizations of SSZ–Fe^{2+}@DSSD. (a) The synthetic procedure of SSZ–Fe^{2+}@DSSD. (b and c) DLS, zeta potential and TEM images of SSZ@DSSD and SSZ–Fe^{2+}@DSSD. (d) Absorbance spectra of free DSSD, SSZ and SSZ–Fe^{2+}@DSSD. (e) The release profile of SSZ from SSZ–Fe^{2+}@DSSD in the absence and presence of GSH (0.1, 1 and 10 mM) for 24 h at 37 °C in pH 7.4 PBS buffer. (f) TEM image of SSZ–Fe^{2+}@DSSD after incubation with 10 mM GSH.

7176 | *J. Mater. Chem. B*, 2021, **9**, 7172–7181

This journal is © The Royal Society of Chemistry 2021

at least for 9 days, and become unstable afterwards, as indicated by increased size and PDI measured by DLS. In contrast, the SSZ–Fe^{2+}@DSSD was stable for at least a period of 21 days, suggesting the critical role of Fe^{2+}-mediated chelation in improving the stability of the SSZ@DSSD system.

To investigate the SSZ loading in the nano-prodrug, the absorbance spectra of SSZ, DSSD and SSZ–Fe^{2+}@DSSD were measured in Fig. 1d and it was found that the absorbance spectrum of SSZ–Fe^{2+}@DSSD contained the characteristic absorption peaks of SSZ at 361 nm and DSSD at 280 nm with a slight deviation. All these results demonstrated that the encapsulation of SSZ and the chelation with Fe^{2+} resulted in a slight change of absorption in the nanoparticles. The SSZ loading efficiency of SSZ–Fe^{2+}@DSSD was determined by the UV-vis method. According to standard curves shown in Fig. S11 (ESI†), the loading efficiency of SSZ in SSZ–Fe^{2+}@DSSD was 23.9 wt%. In order to study the GSH-responsive drug release behavior of SSZ–Fe^{2+}@DSSD, we first evaluated the response of DSSD in 10 mM GSH solution. The DSSD solution was incubated with GSH for 20 min, and then the reaction solution was analysed by HR-MS. As shown in Fig. S12 (ESI†), the molecular ion peak of DSSD and the reaction product DS were simultaneously observed in the MS spectrum. This result indicated that DSSD was sensitive to GSH. After that the release profile of SSZ from the nano-prodrug was measured by HPLC and the result is

displayed in Fig. 1e. Upon incubation with GSH for 24 h, about 85% of SSZ had been released. In contrast, only 10% SSZ was released after incubation in PBS under the same conditions. We also measured the response of SSZ–Fe^{2+}@DSSD to GSH by TEM imaging (Fig. 1f), which indicated that the SSZ–Fe^{2+}@DSSD are aggregated and deformed after incubation with GSH under the same conditions. The DLS also showed that the hydrodynamic diameters of SSZ–Fe^{2+}@DSSD increased upon incubation with GSH. All these results revealed that the GSH could cleave the disulfide bond and disrupt the nanoparticles to release the SSZ in the physiological environment.

To evaluate the catalytic efficiency of SSZ–Fe^{2+}@DSSD to generate the $^{\bullet}$OH under a physiological environment (pH 7.4) and a tumor microenvironment (pH 6.8), the methylene blue (MB) degradation assays were performed in Fig. 2a–c. As shown in Fig. 2a, the decrease of MB absorbance was obviously observed in the presence of SSZ–Fe^{2+}@DSSD in PBS solution (containing H$_2$O$_2$) for 1 h, while the SSZ@DSSD could not induce the MB degradation. With the decrease of the pH value, the absorbance of MB decreased significantly (Fig. 2b), and the color of the reaction solution was also decreased (Fig. 2c). However, SSZ–Fe^{2+}@DSSD without H$_2$O$_2$ exhibited insignificant change. These observations suggested that the SSZ–Fe^{2+}@DSSD could release Fe^{2+} and promote Fenton reaction that induced H$_2$O$_2$ to $^{\bullet}$OH. In addition, the low pH
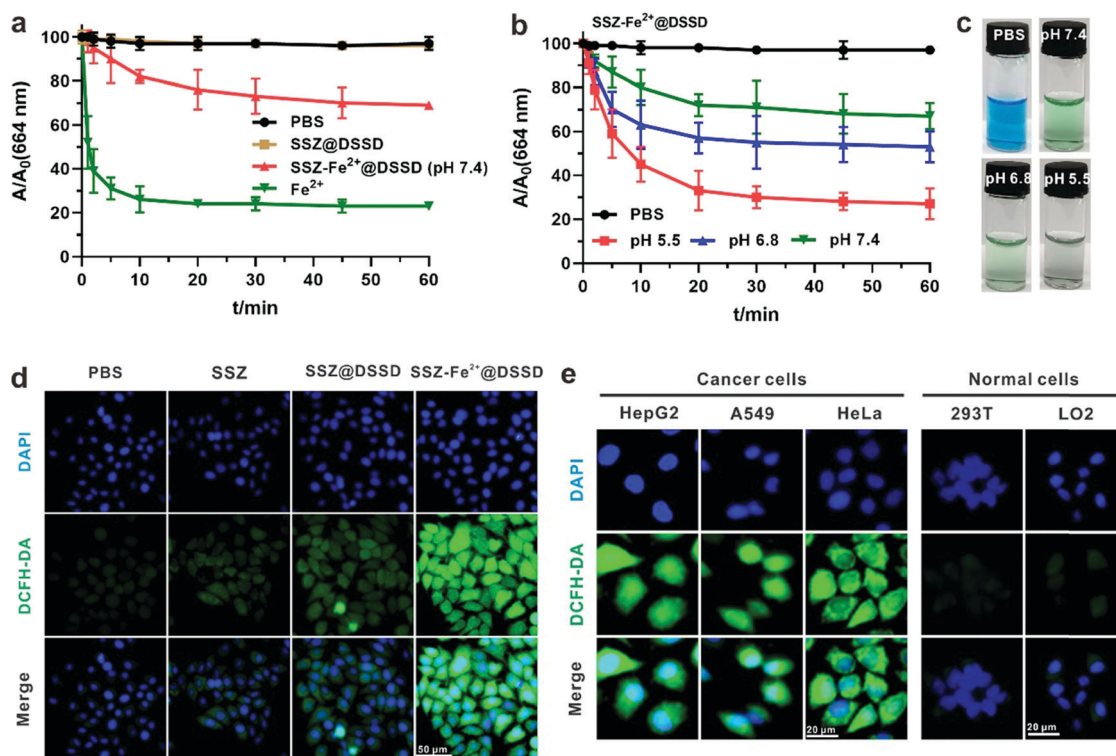
Fig. 2 The $^{\bullet}$OH generation of SSZ−Fe^{2+}@DSSD in PBS buffer and different cells. (a) The $^{\bullet}$OH generation of PBS, Fe^{2+}, SSZ@DSSD, SSZ−Fe^{2+}@DSSD the presence of 1 mM H$_2$O$_2$ and determined by the decrease of MB absorbance at 664 nm. (b) The $^{\bullet}$OH generation of SSZ−Fe^{2+}@DSSD (200 μg mL^{-1}, containing 1 mM H$_2$O$_2$) at different pH values (7.4, 6.8 and 5.5) and determined by MB assays. (c) The photographs of the decrease of MB assays. (d) Fluorescence images of HeLa cells treated with SSZ, SSZ@DSSD and SSZ−Fe^{2+}@DSSD, and ROS generation was stained with DCFH-DA (green) and nuclei was stained with DAPI (blue). (e) Fluorescence images of cancer cells and normal cells incubated with SSZ−Fe^{2+}@DSSD (200 μg mL^{-1}). ROS generation and nuclei were stained with DCFH-DA and DAPI, respectively.

This journal is © The Royal Society of Chemistry 2021

J. Mater. Chem. B, 2021, **9**, 7172–7181 | **7177**

Journal of Materials Chemistry B   Paper

environment could enhance the production of $^{\bullet}OH$, suggesting that the SSZ–Fe^{2+}@DSSD can serve as a ferroptosis inducer.

3.2 Intracellular ROS production and GSH inhibition

Inspired by the catalytic activity of SSZ–Fe^{2+}@DSSD in a low pH microenvironment, the intracellular ROS generation of SSZ–Fe^{2+}@DSSD was explored for using a ROS probe DCFH-DA. Firstly, we explored the ROS generation of the SSZ–Fe^{2+}@DSSD and the other formulations (SSZ, SSZ@DSSD) in HeLa cells. As shown in Fig. 2d, the cells treated with only DCFH-DA (20 μM) had negligible green fluorescence, while the cells that were incubated with SSZ or SSZ@DSSD only showed weak fluorescence. The cells treated with SSZ–Fe^{2+}@DSSD exhibited strong fluorescence after incubation of DCFH-DA, and the quantitative analysis of ROS generation is in consistent with the results in Fig. S13a (ESI†). Moreover, we also assessed ROS generation of cancer cells and normal cells after incubation with SSZ–Fe^{2+}@DSSD using a DCFH-DA probe. In Fig. 2e and Fig. S13b (ESI†), cancer cells (HeLa, A549 and HepG2 cells) displayed a strong green fluorescence intensity, and there was no obvious fluorescence change in the normal cells (293T and LO2 cells), and this result indicated that the SSZ–Fe^{2+}@DSSD exhibited high catalytic specificity in cancer cells because it maintained a high H$_2$O$_2$ level. Recently, many have demonstrated that SSZ can inhibit bio-synthesis intracellular GSH,[2–4] and therefore the evaluation of the GSH level with the different formulations in HeLa cells was performed by using commercial reagents. As shown in Fig. 3a, the level of intracellular GSH was dramatically decreased after incubation with SSZ–Fe^{2+}@DSSD and the other formulations displayed insignificant changes. This result indicated that the SSZ could be released from the nano-prodrug in cancer cells and exhibited the inhibition of GSH production. In order to further verify that SSZ–Fe^{2+}@DSSD can serve as an efficient GSH inhibitor in the system x$_c$$^-$-GSH-GPX4 pathway, we evaluated the expression of the GPX4 protein using western blot (WB) analysis. As shown in Fig. 3b and Fig. S14, S15 (ESI†), an obvious trend for decline in GPX4 expression was observed after the incubation of SSZ–Fe^{2+}@DSSD. Moreover, the relatively low expression of GPX4 protein was also found in SSZ@DSSD and SSZ, while there were no obvious changes in DSSD and Fe^{2+}. All these results indicated that SSZ–Fe^{2+}@DSS could significantly enhance the intracellular oxidative stress by the Fe^{2+}-mediated ROS generation, and disrupted intracellular redox homeostasis by SSZ-mediated GSH depletion.

3.3 *In vitro* ferroptosis-induced cytotoxicity

Then, the effect of ferroptosis nano-drug on the cell viability was performed by using a standard cell viability assay. As shown in Fig. 3c, SSZ–Fe^{2+}@DSSD exhibited higher cytotoxicity to HeLa cells than that of other groups. After incubated with SSZ–Fe^{2+}@DSSD, only about 25% cells kept alive, while there were over 90% cells with SSZ or SSZ@DSSD. We also measured the cell viability assay of HepG2 and A549 cells (Fig. S16a and b, ESI†), which further suggested that the cancer cells exhibited
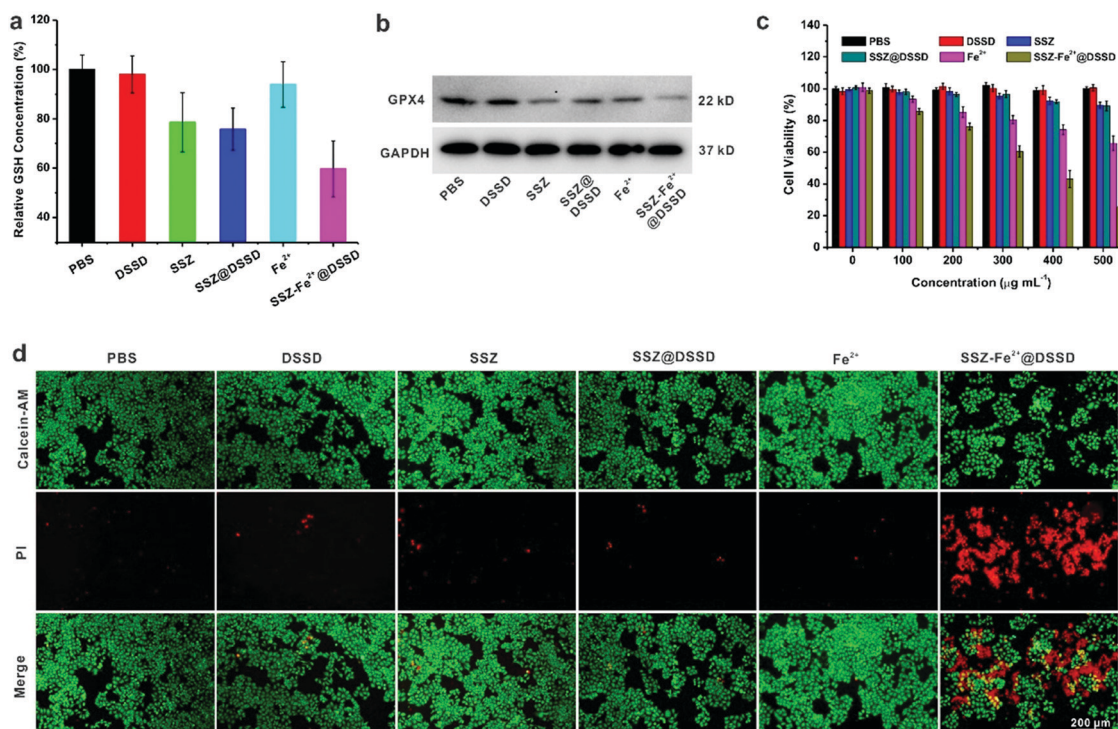

Fig. 3 (a) Intracellular GSH levels of HeLa cells treated with PBS, DSSD, Fe^{2+}, SSZ, SSZ@DSSD, SSZ–Fe^{2+}@DSSD. (b) Expression of GPX4 in HeLa cells treated with PBS, DSSD, Fe^{2+}, SSZ, SSZ@DSSD, SSZ–Fe^{2+}@DSSD for 24 h was detected by western blotting. GAPDH was used as an internal control. (c) The cell viability of HeLa cells at different concentrations (0, 100, 200, 300, 400 and 500 μg mL^{-1}, respectively). (d) The live/dead staining images of HeLa cells after incubation with PBS, DSSD, Fe^{2+}, SSZ, SSZ@DSSD, SSZ–Fe^{2+}@DSSD.

in Fig. 4e, the average body weight of SSZ exhibited a slight weight loss, which might be induced by the systemic toxicity of SSZ. However, the SSZ–Fe^{2+}@DSSD and other groups had no significant change during the treatment process, suggesting the negligible systemic toxicity of the SSZ–Fe^{2+}@DSSD. The pathological H&E staining of tumor sections was also performed for evaluating the therapeutic effects and biosafety of different formulations. As shown in Fig. 4f, the H&E staining of the SSZ–Fe^{2+}@DSSD group displays obvious histological damages, such as nucleus shrinkage and cell apoptosis, while no obvious or only slight damage was observed in tumor slices collected from the other groups. Meanwhile, H&E staining results of the major organs (heart, liver, spleen, lungs and kidneys) showed no obvious damage in the mice in all groups, which proved that SSZ–Fe^{2+}@DSSD display satisfactory biosafety in normal tissues (Fig. S17, ESI†). Finally, the survival rate of the mice administered with different groups was investigated, shown in Fig. 4g, and that of SSZ–Fe^{2+}@DSSD was over 80%, which was much higher than those of other groups. All these results indicated that SSZ–Fe^{2+}@DSSD could achieve a better antitumor efficacy *via* the synergistic ferroptosis while avoiding side effects on normal tissues.

4. Conclusions

In summary, we successfully synthesized a GSH-responsive ferroptosis nano-prodrug SSZ–Fe^{2+}@DSSD *via* a self-assembly strategy. This nano-prodrug was composed of disulfide-bridged levodopa, system x_c^- inhibitor SSZ and Fe^{2+}. The SSZ–Fe^{2+}@DSSD is stable in a normal physiological environment, whereas excessive GSH in tumor tissue breaks the nanostructure and releases the active inhibitor SSZ. Meanwhile, the Fe^{2+} can be released from a nano-prodrug in the acid tumor microenvironment and promote the Fenton reaction, leading to the generation of the •OH for inducing ferroptosis. In addition, the activated SSZ displayed acceptable inhibition of the system x_c^--GSH-GPX4 pathway and amplified the ferroptosis-induced therapy. *In vitro* experiment showed that this nano-prodrug could significantly disrupt intracellular redox homeostasis and induce cancer cells death. More importantly, this nano-prodrug exhibited remarkable antitumor efficacy and insignificant systemic toxicity towards xenograft tumor-bearing mice due to the synergistic effect of SSZ and Fe^{2+}. Therefore, our study provided a generalized prodrug strategy to advance anticancer ferroptosis.

Conflicts of interest

The authors report no conflicts of interest in this work.

Acknowledgements

Notes and references

1 M. Conrad and D. A. Pratt, *Nat. Chem. Biol.*, 2019, **15**, 1137–1147.
2 X. Chen, J. Li, R. Kang, D. J. Klionsky and D. Tang, *Autophagy*, 2020, **26**, 1–28.
3 Z. Shen, J. Song, B. C. Yung, Z. Zhou, A. Wu and X. Chen, *Adv. Mater.*, 2018, **30**, e1704007.
4 C. Liang, X. Zhang, M. Yang and X. Dong, *Adv. Mater.*, 2019, **31**, 1904197.
5 Z. Ye, W. Liu, Q. Zhuo, Q. Hu, M. Liu, Q. Sun, Z. Zhang, G. Fan, W. Xu, S. Ji, X. Yu, Y. Qin and X. Xu, *Cell Proliferation*, 2020, **53**, e12761.
6 C. Ou, W. Na, W. Ge, H. Huang, F. Gao, L. Zhong, Y. Zhao and X. Dong, *Angew. Chem., Int. Ed.*, 2021, **60**, 2–9.
7 W. Bao, X. Liu, Y. Lv, G. Lu, F. Li, F. Zhang, B. Liu, D. Li, W. Wei and Y. Li, *ACS Nano*, 2019, **13**, 260–273.
8 X. Meng, J. Deng, F. Liu, T. Guo, M. Liu, P. Dai, A. Fan, Z. Wang and Y. Zhao, *Nano Lett.*, 2019, **19**, 7866–7876.
9 X. Wan, L. Song, W. Pan, H. Zhong, N. Li and B. Tang, *ACS Nano*, 2020, **14**, 11017–11028.
10 X. Chen, R. Kang, G. Kroemer and D. Tang, *Nat. Rev. Clin. Oncol.*, 2021, **18**, 280–296.
11 N. Kong, W. Tao, X. Ling, J. Wang, Y. Xiao, S. Shi, X. Ji, A. Shajii, S. Gan, N. Kim, A. Duda, T. Xie, O. Farokhzad and J. Shi, *Sci. Transl. Med.*, 2019, **11**, eaaw1565.
12 H. Zheng, J. Jiang, S. Xu, W. Liu, Q. Xie, X. Cai, J. Zhang, S. Liu and R. Li, *Nanoscale*, 2021, **13**, 2266.
13 H. Yan, T. Zou, Q. Tuo, S. Xu, H. Li, A. A. Belaidi and P. Lei, *Signal Transduction Targeted Ther.*, 2021, **6**, 49.
14 Y. Zhang, R. V. Swanda, L. Nie, X. Liu, C. Wang, H. Lee, G. Lei, C. Mao, P. Koppula, W. Cheng, J. Zhang, Z. Xiao, L. Zhuang, B. Fang, J. Chen, S. Qian and B. Gan, *Nat. Commun.*, 2021, **12**, 1589.
15 M. Conrad, S. M. Lorenz and B. Proneth, *Trends Mol. Med.*, 2021, **27**, 113–122.
16 X. Guo, F. Liu, J. Deng, P. Dai, Y. Qin, Z. Li, B. Wang, A. Fan, Z. Wang and Y. Zhao, *ACS Nano*, 2020, **14**, 14715–14730.
17 T. Liu, W. Liu, M. Zhang, W. Yu, F. Gao, C. Li, S. Wang, J. Feng and X. Zhang, *ACS Nano*, 2018, **12**, 12181–12192.
18 J. Y. Cao and S. J. Dixon, *Cell. Mol. Life Sci.*, 2016, **73**, 2195–2209.
19 C. Zhang, Z. Liu, Y. Zhang, L. Ma, E. Song and Y. Song, *Cell Death Dis.*, 2020, **11**, 183.
20 H. Ejima, J. J. Richardson and F. Caruso, *Nano Today*, 2017, **12**, 136–148.
21 C. Wang, H. Sang, Y. Wang, F. Zhu, X. Hu, X. Wang, X. Wang, Y. Li and Y. Cheng, *Nano Lett.*, 2018, **18**, 7045–7051.

7180 | *J. Mater. Chem. B*, 2021, **9**, 7172–7181

This journal is © The Royal Society of Chemistry 2021

22 Y. Jiang, X. Zhao, J. Huang, J. Li, P. K. Upputuri, H. Sun, X. Han, M. Pramanik, Y. Miao, H. Duan, K. Pu and R. Zhang, *Nat. Commun.*, 2020, **11**, 1857.

23 L. Chen, Z. Lin, L. Liu, X. Zhang, W. Shi, D. Ge and Y. Sun, *ACS Biomater. Sci. Eng.*, 2019, **5**, 4861–4869.

24 L. Li, S. Sun, L. Tan, Y. Wang, L. Wang, Z. Zhang and L. Zhang, *Nano Lett.*, 2019, **19**, 7781–7792.

25 C. Xue, M. Li, C. Liu, Y. Li, Y. Fei, Y. Hu, K. Cai, Y. Zhao and Z. Luo, *Angew. Chem., Int. Ed.*, 2021, **60**, 2–12.

26 J. Fu, T. Li, Y. Yang, L. Jiang, W. Wang, L. Fu, Y. Zhu and Y. Hao, *Biomaterials*, 2021, **268**, 120537.

27 R. Xu, J. Yang, Y. Qian, H. Deng, Z. Wang, S. Ma, Y. Wei, N. Yang and Q. Shen, *Nanoscale Horiz.*, 2021, **6**, 348–356.

28 Z. Zhou, X. Wang, H. Zhang, H. Huang, L. Sun, L. Ma, Y. Du, C. Pei, Q. Zhang, H. Li, L. Ma, L. Gu, Z. Liu, L. Cheng and C. Tan, *Small*, 2021, **17**, 2007486.

29 Z. Zhou, B. W. Li, C. Shen, D. Wu, H. C. Fan, J. Q. Zhao, H. Li, Z. Y. Zeng, Z. M. Luo, L. F. Ma and C. L. Tan, *Small*, 2020, **16**, 2004173.

30 Z. Liu, X. Tang, F. Feng, J. Xu, C. Wu, G. Dai, W. Yue, W. Zhong and K. Xu, *J. Mater. Chem. B*, 2021, **9**, 3326–3334.

31 X. Ling, J. Tu, J. Wang, A. Shajii, N. Kong, C. Feng, Y. Zhang, M. Yu, T. Xie, Z. Bharwani, B. M. Aljaeid, B. Shi, W. Tao and O. Farokhzad, *ACS Nano*, 2019, **13**, 357–370.

32 A. Xie, S. Hanif, J. Ouyang, Z. Tang, N. Kong, N. Kim, B. Qi, D. Pantel, B. Shi and W. Tao, *EBioMedicine*, 2020, **56**, 102821.

33 B. Feng, Z. Niu, B. Hou, L. Zhou, Y. Li and H. Yu, *Adv. Funct. Mater.*, 2020, **30**, 1906605.

34 P. Huang, D. Wang, Y. Su, W. Huang, Y. Zhou, D. Cui, X. Zhu and D. Yan, *J. Am. Chem. Soc.*, 2014, **136**, 11748–11756.

35 M. Hou, Y. Gao, X. Shi, S. Bai, X. Ma, B. Li, B. Xiao, P. Xue, Y. Kang and Z. Xu, *Acta Biomater.*, 2018, **77**, 228–239.

36 W. Zhang, Y. Wen, D. He, Y. Wang, X. Liu, C. Li and X. Liang, *Biomaterials*, 2019, **193**, 12–21.

This journal is © The Royal Society of Chemistry 2021

J. Mater. Chem. B, 2021, **9**, 7172–7181 | **7181**